



Cite this: *Chem. Commun.*, 2025, **61**, 1262

Received 29th October 2024,  
Accepted 10th December 2024

DOI: 10.1039/d4cc05762g

[rsc.li/chemcomm](http://rsc.li/chemcomm)

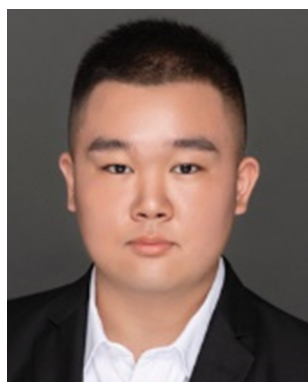
## Electrocatalytic systems for $\text{NO}_x$ upgrading

Shunhan Jia, <sup>ab</sup> Xiaofu Sun, <sup>\*ab</sup> and Buxing Han, <sup>\*abc</sup>

Chemical manufacturing utilizing renewable resources and energy presents a promising avenue toward sustainability and carbon neutrality. Electrocatalytic upgrading of nitrogen oxides ( $\text{NO}_x$ ) into nitrogenous chemicals is a potential strategy for synthesizing chemicals and mitigating  $\text{NO}_x$  pollution. However, this approach is currently hindered by low selectivity and efficiency, limited reaction pathways, and economic challenges, primarily due to the development of suboptimal electrocatalytic systems for  $\text{NO}_x$  upgrading. In this review, we focus on electrocatalytic systems for  $\text{NO}_x$  upgrading and discuss newly developed components, including catalysts, solvents, electrolyzers, and upstream/downstream processes. These advancements enable recent developments in  $\text{NO}_x$  upgrading reactions that yield various products, including green ammonia ( $\text{NH}_3$ ), dinitrogen ( $\text{N}_2$ ), nitrogenous chemicals beyond  $\text{NH}_3$  and  $\text{N}_2$  (e.g., hydroxylamine and hydrazine), and organonitrogen compounds. Additionally, we provide an outlook to highlight future directions in the emerging field of novel electrocatalytic systems for  $\text{NO}_x$  upgrading.

### 1. Introduction

Manufacturing chemicals, fuels, and functional materials from renewable chemical sources and energy represents a sustainable approach to meet the increasing demands of society.<sup>1–5</sup> Nitrogen oxides ( $\text{NO}_x$ )—a group of molecules and ions containing nitrogen and oxygen, such as  $\text{NO}_3^-$ ,  $\text{NO}_2^-$ , and  $\text{NO}$ —pose significant challenges to the global nitrogen cycle. The introduction of  $\text{NO}_x$  from fossil fuel combustion and wastewater discharge is harmful to the environment, biodiversity, and public health. Currently, industries can mitigate  $\text{NO}_x$  pollution by degrading these compounds into dinitrogen ( $\text{N}_2$ ) through



Shunhan Jia received his BS in Chemistry from Nankai University in 2021. He then joined Institute of Chemistry, Chinese Academy of Sciences (CAS) to pursue his PhD under the supervision of Prof. Buxing Han and Prof. Xiaofu Sun. His research interest now focuses on green chemistry and electrocatalytic upgrading of  $\text{NO}_x$ .

**Shunhan Jia**



**Xiaofu Sun**

Xiaofu Sun received his BS in Chemistry from Nankai University in 2011 and MS degree in physical chemistry from Renmin University of China in 2014. He earned his PhD degree at Institute of Chemistry, Chinese Academy of Sciences (CAS) in 2017, and did postdoctoral research at Nanyang Technological University. He has been a professor at the Institute of Chemistry, CAS, since 2019. His current research interest covers utilization and conversion of  $\text{CO}_2$ /  $\text{NO}_x$  applications of green solvents (e.g.  $\text{H}_2\text{O}$ , ionic liquid), and design and synthesis of novel catalysts and catalytic systems.

## Highlight

denitrification processes.<sup>6</sup> However, there is an urgent need for innovative  $\text{NO}_x$  upgrading technologies to contribute to sustainability and carbon neutrality goals, as existing methods do not fully meet demand.<sup>7,8</sup> Upgrading  $\text{NO}_x$  into nitrogenous chemicals using electrocatalytic systems offers a viable solution for reducing  $\text{NO}_x$  pollution while producing valuable chemicals, fuels, and functional materials.<sup>9–11</sup>

ELECTROCATALYTIC upgrading of  $\text{NO}_x$  is inherently complex, involving multiple proton-coupled electron transfer (PCET) processes. For instance, in  $\text{NO}_3^-$  electroreduction,  $\text{NO}_3^-$  can be protonated and subsequently reduced upon adsorption onto the catalyst surface, yielding various nitrogenous intermediates such as  $^*\text{NO}_2$ ,  $^*\text{NO}$ ,  $^*\text{NH}_2\text{OH}$ , etc.<sup>12</sup> The protonation process necessitates the activation of water ( $\text{H}_2\text{O}$ ), which generates active hydrogen species ( $^*\text{H}$ ) that facilitate reduction reactions.<sup>13</sup>  $\text{NO}_3^-$  can be converted into ammonia ( $\text{NH}_3$ ),  $\text{N}_2$ , hydroxylamine ( $\text{NH}_2\text{OH}$ ), and other products. Both  $\text{NH}_3$  and  $\text{NH}_2\text{OH}$  are significant chemical feedstocks, serving as platform molecules for synthesizing additional compounds as nitrogen sources.  $\text{N}_2$  can be released from the solution into the atmosphere without causing pollution.<sup>14</sup> Additionally, nitrogenous intermediates have been reported to couple with carbon-based substrates, leading to the formation of organonitrogen chemicals.<sup>15,16</sup> Current research indicates that  $\text{NO}_x$  can be utilized to synthesize various organonitrogen chemicals, including amino acids, urea, amides, oximes, and amines.

Currently, electrocatalytic upgrading of  $\text{NO}_x$  into various nitrogenous molecules presents challenges, including poor selectivity, low efficiency, and economic viability. Therefore, designing a novel electrocatalytic system is essential to boost  $\text{NO}_x$  upgrading. As is shown in Scheme 1, electrocatalytic systems encompass the catalyst, electrolyte, solvent, electrolyser, and upstream/downstream processes. The structure of the catalyst surface significantly influences the adsorption, conversion, and desorption of intermediates.<sup>17–20</sup> By modifying the

catalyst through alloying, doping, loading, and surface modification, the performance of  $\text{NO}_x$  upgrading can be improved, and product distribution can be tailored. Furthermore, solvents not only dissolve and disperse substrates and electrolytes for the mass transfer and the transport of charge carriers, in  $\text{NO}_x$  upgrading, the solvent (e.g.,  $\text{H}_2\text{O}$ ) also serves as hydrogen source by generating active hydrogen ( $^*\text{H}$ ). Additionally, interactions between cations in electrolytes and intermediates on the catalyst surface can further optimize reactions.<sup>21,22</sup> Many  $\text{NO}_x$  upgrading processes occur at multiphase interfaces, where substrates exist in different phases (gas, aqueous, and organic phases) and demand effective chemical conversion on solid phase catalysts.<sup>23</sup> Consequently, the design of the electrolytic cell, particularly in constructing multiphase interfaces, is crucial for enhancing  $\text{NO}_x$  upgrading. Moreover, the effective separation of products from electrolyte post reactions, along with the development of upstream/downstream processes such as substrate and energy supply, is vital for achieving economically feasible  $\text{NO}_x$  upgrading pathways.

In this highlight, we focus on electrocatalytic systems for  $\text{NO}_x$  upgrading. We first discuss the recent advances in developing components of  $\text{NO}_x$  upgrading electrocatalytic system, including catalysts, solvents, electrolyzers, and upstream/downstream processes. These innovations advance  $\text{NO}_x$  upgrading, yielding a diverse range of products such as green  $\text{NH}_3$ ,  $\text{N}_2$ ,  $\text{NH}_2\text{OH}$ , and other organonitrogen compounds. Additionally, we provide insights into future directions in the rapidly evolving field of innovative electrocatalytic systems for  $\text{NO}_x$  upgrading.

## 2. Electrocatalytic system for $\text{NO}_x$ upgrading

### 2.1 Catalyst

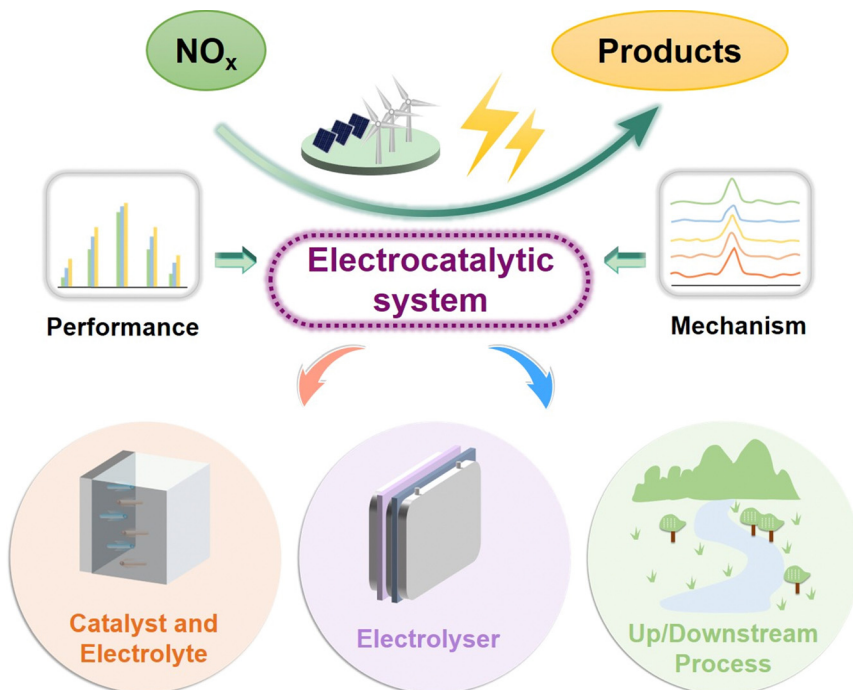
In the electrocatalytic upgrading of  $\text{NO}_x$ , catalysts are critical in facilitating electrochemical reactions among  $\text{NO}_x$ , water, and other reactants at the electrode surface. They effectively lower the energy barrier, improve reaction kinetics, leading to the formation of desired products.<sup>24,25</sup> The fundamental role of a catalyst in this context is to provide active sites where  $\text{NO}_x$  and other reactants can adsorb and undergo reduction *via* electron transfer. An ideal electrocatalyst for  $\text{NO}_x$  upgrading should exhibit high activity, selectivity toward desired products, stability under reaction conditions, and good conductivity to promote efficient electron transfer. Additionally, the catalysts should have a large surface area to maximize active sites and be resistant to poisoning by reaction intermediates or by-products.

Commonly used electrocatalysts for  $\text{NO}_x$  upgrading include noble metals such as platinum (Pt) and palladium (Pd), transition metal oxides, non-precious metal catalysts like iron (Fe) or cobalt (Co)-based compounds, and metal-free materials. While noble metal catalysts typically offer high activity and selectivity, they are costly and prone to deactivation over time.<sup>26</sup> In contrast, transition metal and non-precious metal catalysts provide more cost-effective alternatives but may suffer from lower selectivity or stability. Moreover, catalyst restructuring often occurs during electrocatalytic processes, which can either



Buxing Han

*Buxing Han received his PhD degree at Institute of Chemistry, Chinese Academy of Sciences (CAS) in 1988, and did postdoctoral research from 1989 to 1991 at the University of Saskatchewan, Canada. He has been a professor at the Institute of Chemistry, CAS, since 1993. He is an Academician of CAS and Fellow of Royal Society of Chemistry, a titular member of Organic and Biomolecular Chemistry Division, IUPAC, and was the Chairman of the IUPAC Subcommittee on Green Chemistry from 2008 to 2012. He works in the interdisciplinary area of Physical Chemistry and Green Chemistry. His research interests include properties of green solvent systems and applications of green solvents in chemical reactions and material science.*



Scheme 1 Illustration of electrocatalytic systems for  $\text{NO}_x$  upgrading.

enhance or diminish catalytic performance.<sup>27</sup> Investigating these reconstruction behaviours offers valuable insights into the  $\text{NO}_x$  upgrading mechanism and aids in designing improved catalysts.

## 2.2 Electrolyte and solution

In electrocatalytic  $\text{NO}_x$  upgrading, the choice of supporting electrolytes and solvents plays a pivotal role in modulating reaction conditions, influencing the efficiency and selectivity of the process. Supporting electrolytes are critical for enhancing the conductivity of the electrolyte solution, stabilizing intermediates, and facilitating charge transfer. Commonly used supporting electrolytes include essential cations like  $\text{H}^+$ ,  $\text{Na}^+$ , and  $\text{K}^+$ . These cations can significantly affect the formation, stabilization, and conversion of the intermediates, impacting the overall product distribution. For instance, the cations may alter the local electric field or modify the electrochemical double layer, influencing the key steps in  $\text{NO}_x$  reduction pathway.

While the supporting electrolytes help to stabilize the system and influence reaction kinetics, they can also introduce complexity, such as unwanted ion pairing or competition between cations for active sites on the catalyst. This highlights a growing interest in electrolyte-free electrocatalysis, which could simplify the system, reduce side reactions, and potentially increase product specificity.<sup>28</sup> However, the main challenge in achieving effective  $\text{NO}_x$  upgrading under electrolyte-free conditions is the competition between the  $\text{NO}_x$ -involving reactions and the HER. Without supporting electrolytes, local ionic resistance increases, reducing reaction efficiency. Additionally, lower local pH near the cathode would favour HER over the desired  $\text{NO}_x$ -involving reaction. Despite recent work, such as that by Wang *et al.*,<sup>29</sup> addresses this issue by using a

porous solid electrolyte reactor with a cation shielding effect, electrolyte-free  $\text{NO}_x$  upgrading remains in its early stages, and further research is needed to optimize performance.

In addition,  $\text{H}_2\text{O}$  is the most used solvent in electrocatalytic  $\text{NO}_x$  upgrading, due to its ability to dissolve substrates, support electrolyte dissociation, and crucially, provide a source of hydrogen. The role of water in hydrogen supply is particularly important, as the formation of reactive  $^*\text{H}$  is often a key step in the catalytic cycle. Moderately activating water to produce  $^*\text{H}$  is essential, as excessive activation leads to the undesired side reactions such as hydrogen evolution reaction (HER), which lowers the faradaic efficiency. Conversely, insufficient activation might hinder the availability of hydrogen species, limiting the reduction of  $\text{NO}_x$  intermediates.

## 2.3 Electrolyser

Electrocatalytic  $\text{NO}_x$  upgrading is typically performed in electrolytic cells, where the structure and design of the cell significantly impact reaction efficiency and scalability. One commonly used configuration is the H-type electrolytic cell, which features a diaphragm to separate the anode and cathode compartments. This separation helps prevent the oxidation of reduction products formed at the cathode by the anodic reactions. While effective for lab-scale experiments, H-type cells have limitations, including lower scalability, inefficient mass transport, and higher internal resistance due to the diaphragm, which can hinder performance for large-scale applications. To address these limitations, flow electrolysis cells have been developed.<sup>30,31</sup> These cells allow for the continuous flow of electrolyte and gases through the cell, enhancing mass transport and making them more suitable for scaling up production. Flow cells also often incorporate gas

## Highlight

diffusion layers (GDLs), which facilitate the efficient introduction of gaseous reactant such as NO improving the contact between the gas, electrolyte, and catalyst.<sup>32</sup> This design is particularly advantageous for reactions involving gases, as it enables better management of reactant delivery and product removal.

Another innovative cell design is the diaphragm-free electrolytic cell, which eliminates the need for expensive membranes, reducing the complexity of the setup and lowering cell voltage. However, without a diaphragm, there is an increased risk of side reactions, such as the reoxidation of reduced  $\text{NO}_x$  species at the anode. Optimizing diaphragm-free cells requires careful selection and design of catalysts that promote selective  $\text{NO}_x$  reduction while minimizing undesirable side reactions.<sup>33,34</sup> New catalytic materials that enhance selectivity are being investigated to improve the overall efficiency of these systems.

#### 2.4 Upstream and downstream process

In electrocatalytic  $\text{NO}_x$  upgrading, upstream and downstream processes play crucial roles in achieving an integrated and sustainable system. The upstream processes involve the acquisition of  $\text{NO}_x$ , which can be captured from diverse sources such as exhaust gases, wastewater, or generated *via* biological fermentation and plasma air oxidation. In addition, coupling  $\text{NO}_x$  electrocatalytic upgrading with renewable energy harvesting, such as integrating electrocatalytic devices with photovoltaic systems or advancing photocatalytic technologies, creates a more sustainable approach by utilizing green energy and renewable nitrogenous sources.<sup>30,35</sup> Downstream processes, after the  $\text{NO}_x$  conversion reaction, offer opportunities to further enhance the economic benefits of the system by generating high-value products through additional reactions or by employing separation techniques to obtain high-purity products.

As a result, catalysts, solvents, electrolytic cells, and upstream and downstream processes collectively drive the efficiency and sustainability of electrocatalytic  $\text{NO}_x$  conversion. Their synergistic cooperation ensures that each step—acquiring  $\text{NO}_x$ , driving the reaction with renewable energy, and refining the products—contributes to a fully integrated and optimized  $\text{NO}_x$  upgrading system.

### 3. Upgrading of $\text{NO}_x$ to value-added chemicals

#### 3.1 Green ammonia

Efficiently converting  $\text{NO}_x$  to green  $\text{NH}_3$  not only mitigates these harmful emissions but also offers a pathway to recycle nitrogen for  $\text{NH}_3$  production. The moderate adsorption of nitrogenous intermediates on the catalyst during the reduction of  $\text{NO}_x$  to  $\text{NH}_3$  is crucial for improving electrochemical performance. Recently, Lu and co-workers designed a series of Pd-based bimettallene (PdM, where M = Fe, Co, Ni, Cu) and applied them as catalysts for  $\text{NO}_3^-$  electroreduction to  $\text{NH}_3$ .<sup>36</sup> The ultra-thin nanosheet structure of these bimettallene facilitated the exposure of active sites. The doping of transition metals broke the electronic balance on the surface and upshifted the d-band

center of Pd metallene, optimizing the adsorption of intermediates (Fig. 1(a)). Among these bimettallene, the anisotropic electronic characteristics of the transition metals led to the  $\text{NO}_3^-$  electroreduction activity in the order of  $\text{PdCu} > \text{PdCo} \approx \text{PdFe} > \text{PdNi} > \text{Pd}$ . As is shown in Fig. 1(b), the PdCu bimettallene achieved an outstanding  $\text{NH}_3$  yield rate of  $295 \text{ mg h}^{-1} \text{ mg}_{\text{cat}}^{-1}$  and a faradaic efficiency (FE) of 90.9%. The proper combination of elements in PdCu bimettallene resulted in a moderate adsorption ability of  $^*\text{NO}_3$  and  $^*\text{NO}$ , enhanced NO activation, and reduced HER activity. The hydrogenation of NO to NOH was the rate-determining step, and PdCu had the lowest energy barrier for this step. The adsorption energies of  $^*\text{NO}_3$  and  $^*\text{NO}$  on PdCu were close to the optimal values (Fig. 1(c)), preventing catalyst deactivation and facilitating the hydrogenation process. In addition to the adsorption energy of nitrogenous intermediates, their adsorption configuration also has a significant impact on  $\text{NO}_x$  reduction.<sup>37</sup> For instance, through theoretical calculations, Zn was identified as a promising dopant for Cu catalysts to boost  $\text{NO}_3^-$  electroreduction to  $\text{NH}_3$ .<sup>38</sup> Zn-doped Cu nanosheets exhibited excellent performance, achieving a maximum  $\text{NH}_3$  FE of up to 98.4% (Fig. 1(d)). The catalyst also showed good cycling stability and maintained a high FE over a wide potential and  $\text{NO}_3^-$  concentration range. Zn doping modulated the adsorption strength of intermediates, enhanced nitrite conversion (Fig. 1(e)), changed the  $^*\text{NO}$  adsorption configuration to bridge adsorption (Fig. 1(f) and (g)), and decreased the energy barrier, leading to the enhanced catalytic performance. Besides doping-induced adsorption configuration transformation, recent research by Zhang *et al.* has demonstrated that,<sup>39</sup> on the  $\text{RuIn}_3/\text{C}$  catalyst, the adsorption configuration of  $^*\text{NO}$  changes under pulse electrolysis conditions compared to conventional constant-potential electrolysis, leading to enhanced  $\text{NO}_x$ -to- $\text{NH}_3$  performance.

The precise activation of  $\text{H}_2\text{O}$  as a hydrogen source for the reduction of  $\text{NO}_x$  to  $\text{NH}_3$  urgently needs to be achieved. The Yu group demonstrated a sulphur-doped copper nanorod arrays (Cu-S NAs) electrocatalyst prepared *via* an electrochemical conversion strategy for  $\text{NO}_3^-$  reduction (Fig. 1(h)).<sup>40</sup> An excellent FE of  $\text{NH}_3$  (98.3%) and significant decrease of FE of  $\text{NO}_2^-$  (1.4%) were achieved on Cu-S NAs, compared with those of counterpart catalysts as illustrated in Fig. 1(i). The enhanced selectivity of Cu-S NAs was attributed to the optimized hydrogen affinity and decreased hydrogenation energy barrier. A small amount of S doping on Cu surface could promote the kinetics of dissociation to active hydrogen, and the optimized hydrogen affinity validly decreased the hydrogenation kinetic energy barrier of  $^*\text{NO}$ , leading to an enhanced  $\text{NH}_3$  selectivity (Fig. 1(j)).

In addition to adjusting the electronic structure of the catalyst to moderate intermediates, optimization based on the electrode interface environment also contributes to  $\text{NO}_x$  reduction. Yu *et al.* proposed an effective strategy to modulate the electrolyte microenvironment in electrical double layer (EDL) by mediating alkali metal cations in the electrolyte to enhance the electrochemical performance of  $\text{NO}_3^-$  reduction to  $\text{NH}_3$ .<sup>41</sup> With Cu foam used as a model catalyst, as is demonstrated in Fig. 1(k), the performance of  $\text{NH}_3$  generation in

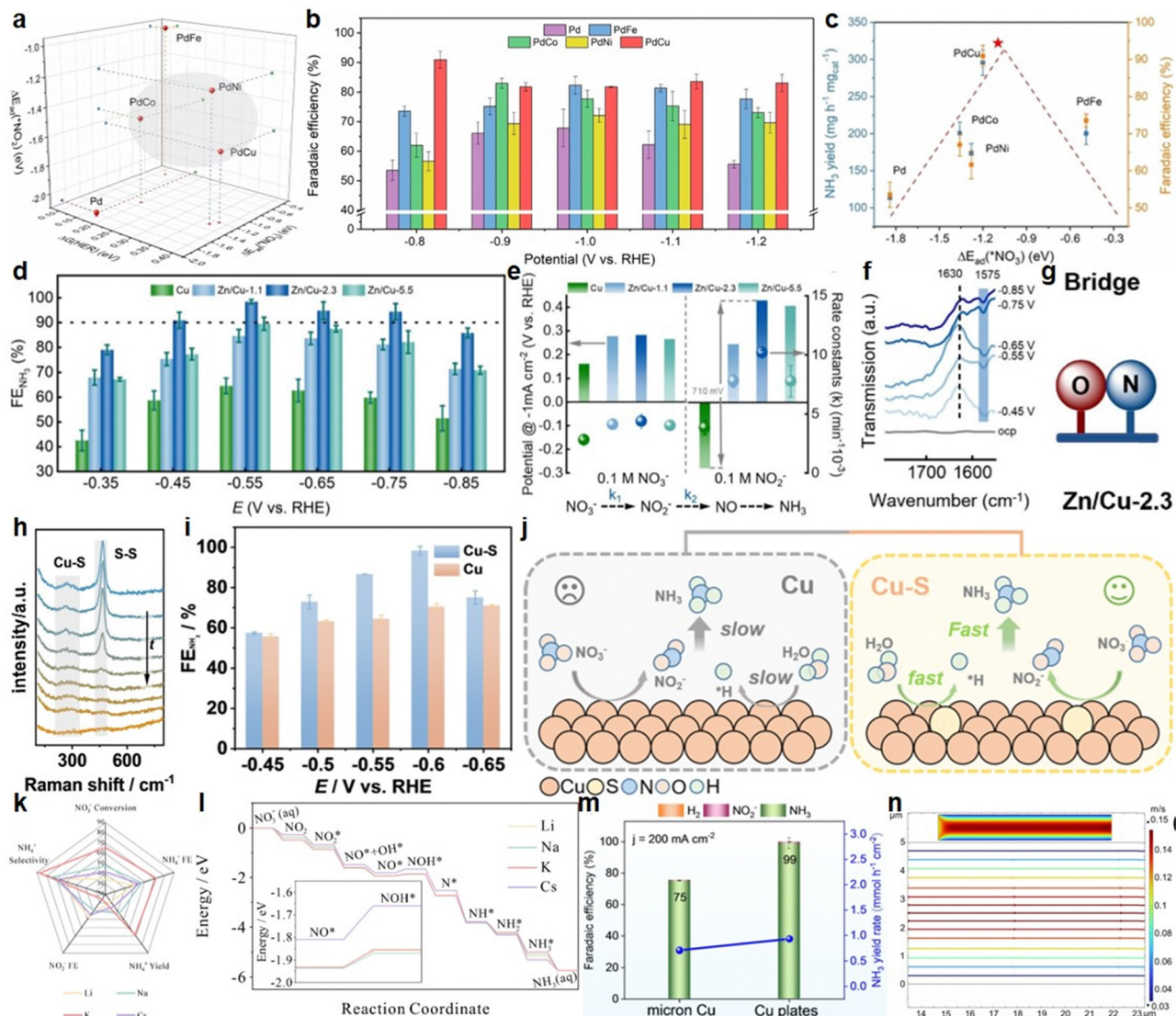


**Fig. 1** (a) The adsorption energy of  $^*\text{NO}_3$  and  $^*\text{NO}_2$  and HER Gibbs free energy on Pd with different dopants. (b)  $\text{NH}_3$  FE of Pd, PdFe, PdCo, PdNi and PdCu. (c) The adsorption energy of  $^*\text{NO}_3$  and  $\text{NO}_3^-$  reduction performance on different Pd metallene. Reproduced with permission from ref. 36. (d)  $\text{NH}_3$  FE of Zn/Cu-2.3 catalyst. (e) Onset potentials and reaction constants ( $k_1$  for  $\text{NO}_3^-$ -to- $\text{NO}_2^-$  and  $k_2$  for  $\text{NO}_2^-$ -to- $\text{NO}$ ) of different Zn-Cu catalysts. (f) *In situ* ATR-FTIR spectra of Zn/Cu-2.3 during  $\text{NO}_3^-$  reduction. (g) Illustration of the configuration of  $^*\text{NO}$  on Zn/Cu-2.3. Reproduced with permission from ref. 38. (h) *In situ* Raman spectra for the electrochemical synthesis of Cu-S NAs. (i)  $\text{NH}_3$  FE and (j) the corresponding mechanism of Cu-S NAs and Cu NAs. Reproduced with permission from ref. 40. (k) Electrochemical performance and (l) the pathway diagram performance of  $\text{NO}_3^-$  reduction using different alkali metal cations. Reproduced with permission from ref. 41. (m)  $\text{NH}_3$  FE and yields of Cu plates and micron Cu. (n) Velocity field streamline for the Cu plates in a steady state. Reproduced with permission from ref. 42.

electrolytes containing different cations followed the trend of  $\text{Li}^+ < \text{Cs}^+ < \text{Na}^+ < \text{K}^+$ . In 1 mol L<sup>-1</sup> KOH electrolyte, 99% of  $\text{NO}_3^-$  conversion and 98% of  $\text{NH}_3$  FE were achieved. Alkali metal cations can tune the electrostatic potential (ESP) distribution and protons transport in EDL. In the presence of  $\text{K}^+$ , the ESP in EDL was more negative and the energy barrier for protons to cross EDL was lower, facilitating faster protons transport to the catalytic surface and thereby promoting the subsequent hydrogenation of intermediates (Fig. 1(j)). Recently, Lv and co-workers constructed a steady fluid field along the surface of 2D Cu plates with a uniform sheet-like morphology and nanosized thickness, exhibiting excellent electrochemical performance.<sup>42</sup> 2D Cu plates

achieved a superior  $\text{NH}_3$  FE of 99%, exceptional long-term electrolysis for 120 h at 200 mA cm<sup>-2</sup>, and a record-high yield rate of 3.14 mmol cm<sup>-2</sup> h<sup>-1</sup> (Fig. 1(m)). In a Zn- $\text{NO}_3^-$  battery system, it provided a power density of 12.09 mW cm<sup>-2</sup> and  $\text{NH}_3$  FE of 85.4%. The steady fluid field shown in Fig. 1(n) was found to play a critical role in determining the fluid velocity field and renewal of catalytic active sites, which contributed to the high efficiency of  $\text{NH}_3$  production.

Coupling electrocatalytic systems of  $\text{NO}_x$  reduction to  $\text{NH}_3$  with anodic oxidation reactions, renewable energy harvesting (integrating with photovoltaic devices or conducting photoelectrochemical catalysis) and product separation can reduce

## Highlight

energy input and enhance product value. Recently, Hong and co-workers developed a photoconductive organic network for  $\text{NO}_3^-$  reduction to  $\text{NH}_3$ , which was formed by chemically interweaving poly(2-methoxy-5-propyloxysulfonate phenylene vinylene) (PPV) in a covalent scaffold and functionalized with a Cu catalyst.<sup>43</sup> The resulting photoelectrode (PPV-Cu), as is shown in Fig. 2(a), exhibited excellent performance, with a photocurrent density of  $8.5 \text{ mA cm}^{-2}$  and a FE of  $\text{NH}_3$  at 95% under  $100 \text{ mW cm}^{-2}$  solar irradiation, corresponding to an external quantum efficiency of 13%. In a tandem system with a  $\text{BiVO}_4$  photoanode, the system could simultaneously convert  $\text{NO}_3^-$  to  $\text{NH}_3$  and oxidize  $\text{H}_2\text{O}$  to  $\text{O}_2$  (Fig. 2(b)). The efficient generation of charge carriers at the interfaces between the

organic electron-donating photoconductor and electron-accepting catalyst upon illumination enabled the enhanced charge separation for photoelectrochemical catalysis. In addition, Liu *et al.* developed a template-free strategy was to prepare two-dimensional high-entropy oxide (HEO) nanoplates with single-crystallinity and penetrated mesoporosity.<sup>44</sup> The single-crystalline mesoporous HEO (SC-MHEO), exhibited remarkable performance in the 5-hydroxymethylfurfural oxidation reaction for efficient biomass upgrading. Additionally, with nitrate reduction as a coupling cathode reaction, SC-MHEO realized the concurrent electrosynthesis of value-added 2,5-furandicarboxylic acid and  $\text{NH}_3$  in a two-electrode cell (Fig. 2(c) and (d)).

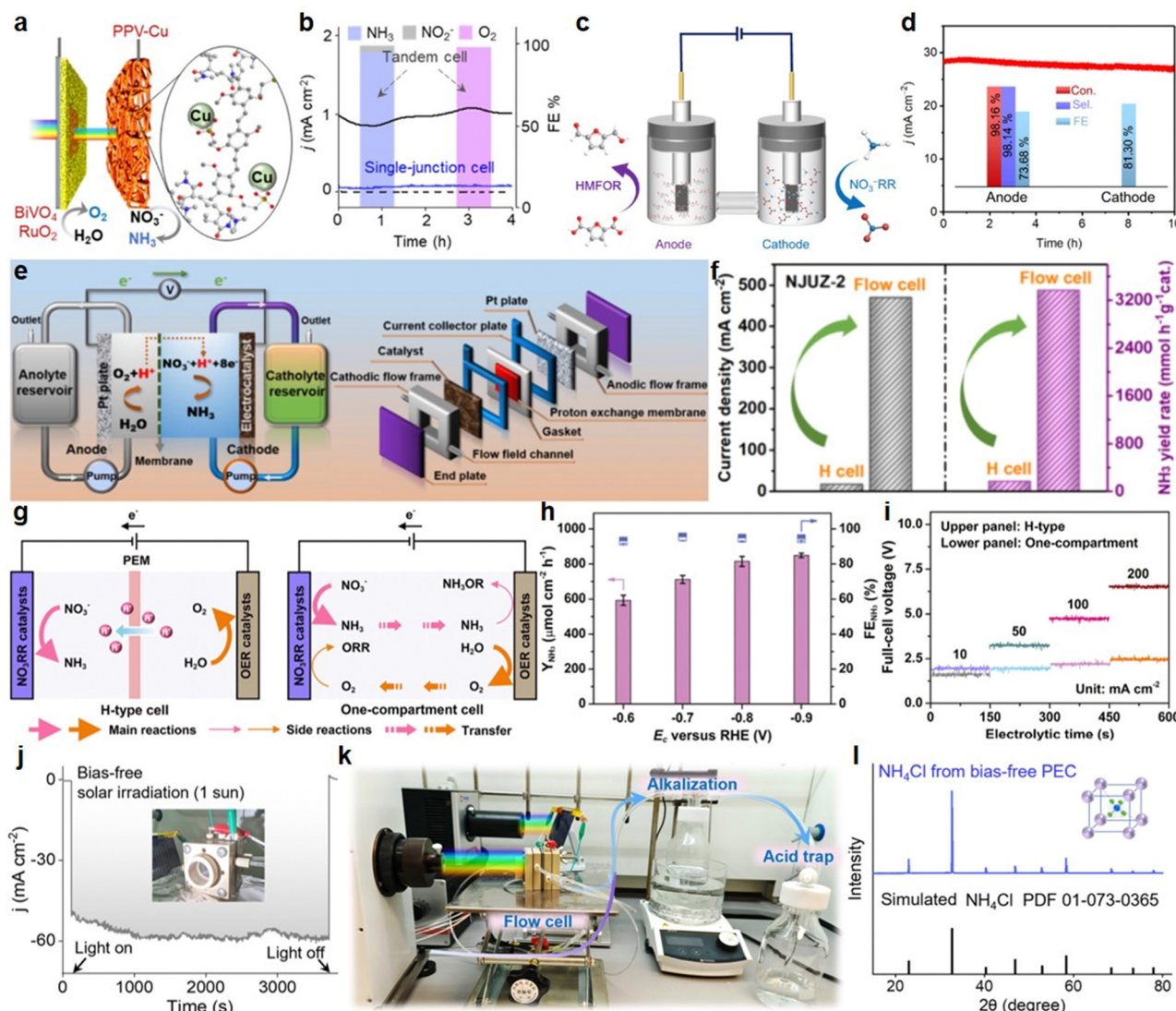


**Fig. 2** (a) Integrated system of PPV-Cu and  $\text{BiVO}_4$  and (b) the corresponding FE of  $\text{NH}_3$  and  $\text{O}_2$  under solar irradiation. Reproduced with permission from ref. 43. (c) Two-electrode coupling system integrating  $\text{NO}_3^-$  reduction with biomass upgrading. (d) Electrochemical performance of the integrated system. Reproduced with permission from ref. 44. (e) Illustration of the flow cell system for  $\text{NO}_3^-$  reduction and (f) the comparison of electrochemical performance using H-cell and flow cell. Reproduced with permission from ref. 31. (g) Illustration of  $\text{NO}_3^-$  reduction in H-cell and flow cell and one-compartment cell. (h) Performance of  $\text{NH}_3$  generation in one-compartment cell. (i) Comparison of full-cell voltage using different cells. Reproduced with permission from ref. 45. (j) Current density of the (k) integrated photoelectrochemical system. (l) Isolated  $\text{NH}_4\text{Cl}$  product generated from  $\text{NO}_3^-$  reduction. Reproduced with permission from ref. 30.

The design of electrolytic cells beyond typical H-cell is of great importance. The Jin group designed and synthesized two poly-nuclear cobalt-cluster-based coordination polymers (CPs), NJUZ-2 and NJUZ-3, were for efficient  $\text{NO}_3^-$ -to- $\text{NH}_3$  electroreduction.<sup>31</sup> These CPs posed distinct coordination motifs with well-defined porosity, high-density catalytic sites, accessible mass transfer channels, and nanoconfined chemical environments, leading to the remarkable catalytic activities of NJUZ-2 for  $\text{NO}_3^-$ -to- $\text{NH}_3$ . NJUZ-2 achieved an optimal FE of 98.5% and high long-term durability for  $\text{NH}_3$  production, which was attributed to the preferential adsorption of  $\text{NO}_3^-$  and the reduction in energy input required for the hydrogenation of  $^*\text{NO}$  and  $^*\text{NO}_2$  intermediates. In a flow cell (Fig. 2(e)) at an industrially relevant current density of  $469.9 \text{ mA cm}^{-2}$ , NJUZ-2 achieved a high  $\text{NH}_3$  yield rate of up to  $3370.6 \text{ mmol h}^{-1} \text{ g}_{\text{cat}}^{-1}$ , which is significantly improved compared with the performance in H-cell as is illustrated in Fig. 2(f). The Gao group presented efficient membraneless electrochemical synthesis of  $\text{NH}_3$  from  $\text{NO}_3^-$  using a Co-Co system, which was selected through screening for its excellent  $\text{NO}_3^-$  and  $\text{H}_2\text{O}$  oxidation activities, along with negligible  $\text{O}_2$  reaction and  $\text{NH}_3$  oxidation (Fig. 2(g)).<sup>45</sup> As is shown in Fig. 2(h) and (i), at  $200 \text{ mA cm}^{-2}$ , the full-cell voltage of the membraneless system (2.5 V) was 4 V lower than that of the membrane system (6.5 V), with significant energy savings. A maximum  $\text{NH}_3$  yield rate of  $1500.9 \text{ } \mu\text{mol cm}^{-2} \text{ h}^{-1}$  was achieved at  $-0.9 \text{ V}$  with a  $\text{NH}_3$  FE of 92.6%. In addition, the pulsed process induces reversible surface reconstruction, generating and restoring active  $\text{Co}^{\text{III}}$  species at the working electrode and forming favourable  $\text{Co}_3\text{O}_4/\text{CoOOH}$  at the counter electrode, which further improved the  $\text{NO}_3^-$ -to- $\text{NH}_3$  conversion and hindered side reactions. Shan and co-workers developed an organic p-n junction approach for fabricating molecular photoelectrodes integrated with a CuCo catalyst to convert solar energy and  $\text{NO}_3^-$  into  $\text{NH}_3$ , which exhibited excellent electrochemical performance.<sup>30</sup> As is shown in Fig. 2(j), the system based-on p-n junction achieved an external quantum efficiency (EQE) of 57% and an internal quantum efficiency (IQE) of 86% for  $\text{NH}_3$  production under solar irradiation. The photogenerated electrons and holes were spatially separated at the n-type perylene diimide (PDI) and p-type poly(3,4-ethylenedioxythiophene) (PEDOT) components of the p-n junction with a quantum yield of 90%. The high-flux photogenerated electrons at PDI were rapidly transferred to the CuCo catalyst for  $\text{NO}_3^-$  reduction. Consequently, in a flow-cell setup coupled with a silicon solar cell and under bias-free conditions, it generated a photocurrent of  $57 \text{ mA cm}^{-2}$  and an EQE for  $\text{NH}_3$  production of 52% (Fig. 2(k)). The high-purity ammonium chloride ( $\text{NH}_4\text{Cl}$ ) product shown in Fig. 2(l) was separated from electrolyte.

### 3.2 Dinitrogen

The electroreduction of  $\text{NO}_x$  to  $\text{N}_2$  offers a compelling approach to address nitrogen-pollution, which is a significant environmental issue. Since traditional methods for removing  $\text{NO}_x$ , such as thermal-chemical treatments, face limitations including high energy consumption and operational complexity. Reduction of  $\text{NO}_x$  to  $\text{N}_2$  presents an environmentally friendly alternative and offers the potential for integration with

renewable energy sources.<sup>46</sup> Recently, Wang *et al.* fabricated a mechanically flexible 2D MXene ( $\text{Ti}_3\text{C}_2\text{T}_x$ ) membrane with multi-layered nanofluidic channels was fabricated, which exhibited high selectivity for  $\text{NO}_3^-$  reduction to  $\text{N}_2$  (82.8%) with a high  $\text{N}_2$  FE of 72.6% for  $\text{NO}_3^-$  reduction to  $\text{N}_2$  at a very low electrical cost of  $0.28 \text{ kWh m}^{-3}$  (Fig. 3(a) and (b)).<sup>47</sup> The water flowing through the MXene nanosheets facilitated the mass transfer of nitrate onto these sites and the defects on the MXene nanosheet surfaces played an important role to reduce  $\text{NO}_3^-$  (Fig. 3(c)). The relatively low desorption energy barrier for the release of adsorbed  $\text{N}_2$  compared to that for the adsorbed  $\text{NH}_3$  contributed to the high selectivity for  $\text{N}_2$  production. Yang and co-workers reported a single atom alloy (SAA) catalyst,  $\text{Ru}_1\text{Ni}$ , which showed remarkable performance for  $\text{NO}_3^-$  reduction to  $\text{N}_2$  (Fig. 3(d)), in which the electron transfer from Ni to Ru and enhanced nitrate adsorption. The promotion of  $\text{NO}_3^-$  activation on the Ru site and accelerated hydrogenation of nitrogenous intermediates on the Ni substrate.<sup>29</sup> In the flow-cell shown in Fig. 3(e), The  $\text{Ru}_1\text{Ni}$  SAA catalyst exhibits high  $\text{NO}_3^-$ - $\text{N}$  conversion ( $\approx 93\%$ ) and  $\text{N}_2$  selectivity ( $\approx 99\%$ ) with a removal capacity of  $11.1 \text{ mg L}^{-1} \text{ h}^{-1} \text{ cm}^{-2}$  and 20 cycles stability (Fig. 3(f)), in which the current density was significantly higher than that in single cell. The Zhu group developed a flow-through zero-gap electrochemical reactor was for  $\text{NO}_3^-$  reduction to  $\text{NH}_3$ , using a reconstructed  $\text{Cu}(\text{OH})_2$  cathode with a 3D network structure.<sup>33</sup> The reactor exhibited excellent electrochemical performance, achieving 100%  $\text{NO}_3^-$  conversion and 80.36%  $\text{N}_2$  selectivity, along with rapid reduction kinetics of  $0.077 \text{ min}^{-1}$ . The mass transport and current utilization efficiency were significantly enhanced by shortening the inter-electrode distance. The *in situ* reconstruction of the  $\text{Cu}(\text{OH})_2$  cathode to form  $\text{Cu}/\text{Cu}_2\text{O}$  was crucial for efficient nitrate reduction. The highly selective conversion of  $^*\text{NO}$  to  $^*\text{N}$  and the N-N coupling step were facilitated by improving the coverage of the key intermediate  $^*\text{N}$ .

### 3.3 Nitrogenous chemicals beyond ammonia and dinitrogen

$\text{NO}_x$  electroreduction to products beyond  $\text{N}_2/\text{NH}_3$ , such as  $\text{NH}_2\text{OH}$ , is challenging because key intermediates tend to undergo excessive reduction, favouring the formation of  $\text{N}_2/\text{NH}_3$ . However, recent advances have demonstrated that  $\text{NO}_x$  electroreduction can yield products beyond  $\text{N}_2/\text{NH}_3$ , with  $\text{NH}_2\text{OH}$  being efficiently produced.

$\text{NH}_2\text{OH}$  is a valuable chemical raw material with important applications in fuels, pharmaceuticals, and agrochemicals. Traditional methods for synthesizing  $\text{NH}_2\text{OH}$  face limitations such as harsh conditions, environmental pollution, and high energy consumption. In contrast, electrochemical  $\text{NO}_x$ -to- $\text{NH}_2\text{OH}$  under mild conditions using renewable energy offers a more sustainable alternative. We demonstrated the electrochemical synthesis of  $\text{NH}_2\text{OH}$  *via* ketone-mediated  $\text{NO}_3^-$  reduction as is illustrated in Fig. 4(a).<sup>48</sup> A metal-organic-framework-derived Cu catalyst ( $\text{Cu}_x\text{C}_y\text{O}_z@600$ ) was developed and exhibited remarkable performance. It achieved an excellent FE of 47.8% and a corresponding formation rate of  $34.9 \text{ mg h}^{-1} \text{ cm}^{-2}$  for cyclopentanone oxime (CP-O) formation (Fig. 4(b)). Through hydrolysis of CP-O, a significantly higher concentration of  $96.1 \text{ mmol L}^{-1} \text{ NH}_2\text{OH}$  could be stabilized in the

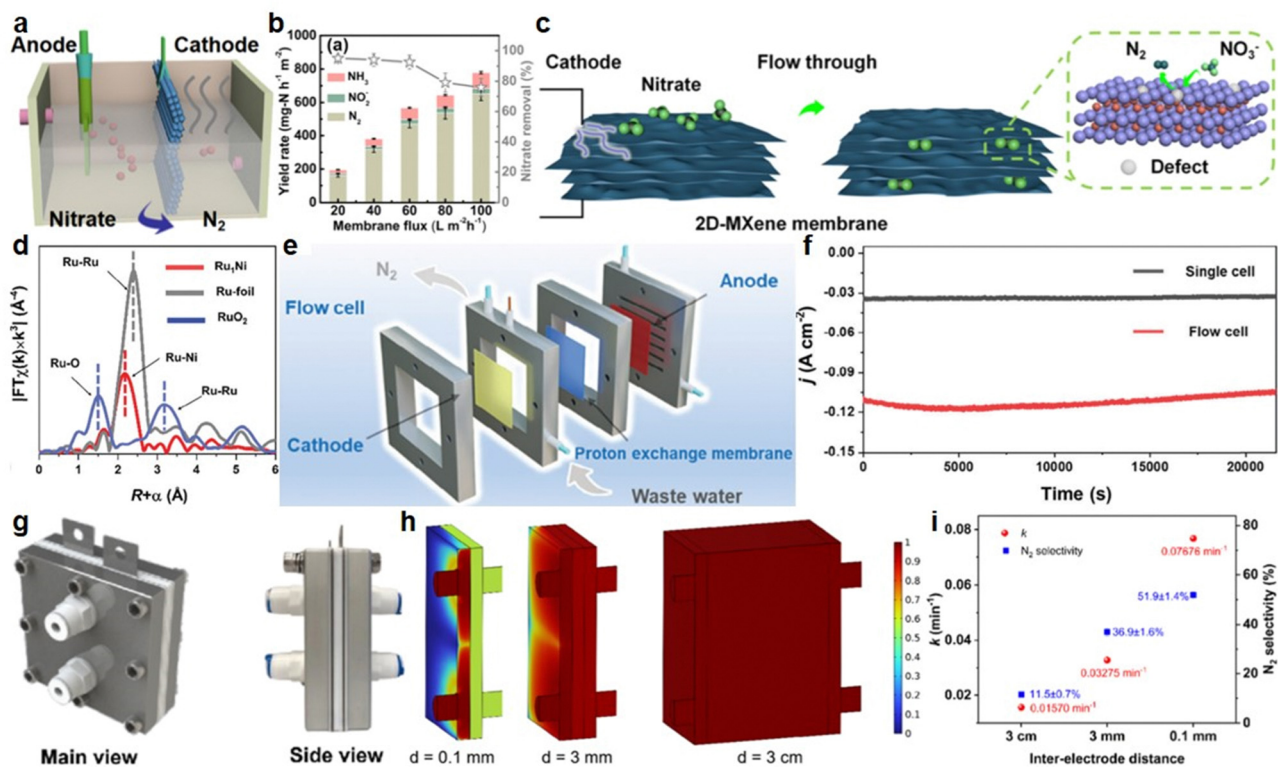


Fig. 3 (a) Illustration of the continuous-flow cell and the corresponding  $\text{N}_2$  yield rates and  $\text{NO}_3^-$  removal per order reduction. (c) The mass transfer process of  $\text{NO}_3^-$  in catalyst pores. Reproduced with permission from ref. 47. (d) EXAFS spectra of  $\text{Ru}_1\text{Ni}$  SAA in the  $R$  space of Ru K-edge. (e) The customized flow cell and (f) the corresponding long-term stability assessment of the  $\text{Ru}_1\text{Ni}$  SAA for  $\text{NO}_3^-$  removal. Reproduced with permission from ref. 29. (g) Photography of electrochemical cell with zero-gap. (h) Density distribution of  $\text{NO}_3^-$  and (i) electrochemical performance in flow-through electrochemical reactors with different gap. Reproduced with permission from ref. 33.

solution with a 99.9% CP-O conversion and a 96.2% HA selectivity. The reaction proceeded through a series of steps including the chemical adsorption of  $\text{NO}_3^-$  on the catalyst surface to form  $^*\text{NO}$ , followed by protonation and reduction steps to form various intermediates, and finally leading to the formation of  $\text{NH}_2\text{OH}$  and its capture by ketone to form CP-O (Fig. 4(c) and (d)). The coexistence of  $\text{Cu}^0$  and  $\text{Cu}^+$  on the catalyst surface was beneficial for the protonation and reduction of  $^*\text{NO}$  and  $^*\text{NH}_2\text{OH}$  desorption, which enhanced the production of  $\text{NH}_2\text{OH}$ . Zhang and co-workers designed and prepared Co single-atom catalysts (SACs) and Co nanoparticles (Co NPs).<sup>49</sup> As is shown in Fig. 4(e), Co SACs showed excellent  $\text{NH}_2\text{OH}$  selectivity (NH<sub>2</sub>OH FE of 81.3%) from NO electroreduction under mild conditions, while Co NPs were more inclined to generate  $\text{NH}_3$  (NH<sub>3</sub>FE of 92.3%). It was found that the linear adsorption of NO on isolated Co sites in Co SACs, which was proved in Fig. 4(f), enabled the formation of  $\text{NH}_2\text{OH}$ , while the bridge adsorption of NO on adjacent Co sites in Co NPs induced the production of  $\text{NH}_3$  (Fig. 4(g)). Zeng group presented an innovative approach for hydroxylamine synthesis using air as the nitrogen source and  $\text{H}_2\text{O}$  as the hydrogen source.<sup>50</sup> A plasma-electrochemical cascade pathway (PECP) was developed, which involved two main steps. Firstly, plasma treatment of ambient air and water produced a  $\text{NO}_3^-$  solution with a concentration of up to  $120.1 \text{ mol L}^{-1}$ . Then, the obtained

$\text{NO}_3^-$  was selectively converted to  $\text{NH}_2\text{OH}$  through electroreduction, using a bismuth-based electrode (Bi film/CFP). Bi film/CFP exhibited an excellent FE for  $\text{NH}_2\text{OH}$  reaching 81.0% and a high hydroxylamine yield rate of  $713.1 \mu\text{mol cm}^{-2} \text{ h}^{-1}$ . A very high selectivity for  $\text{NH}_2\text{OH}$  of 95.8% was also achieved. On the Bi(012) facet of Bi film/CFP electrode, the potential-determining step for the formation of both  $\text{NH}_2\text{OH}$  and  $\text{NH}_3$  was the protonation process of  $^*\text{NO}$  into the adsorbed NHO intermediate. However, the desorption of  $^*\text{NH}_2\text{OH}$  into  $\text{NH}_2\text{OH}$  was more thermodynamically favourable than the dissociation into  $^*\text{NH}_2$  and  $^*\text{OH}$ , leading to the selective formation of  $\text{NH}_2\text{OH}$ .

Xiao and co-workers utilized an improved constant potential simulation method and microkinetic model to understand NO reduction to  $\text{NH}_3$  and  $\text{NH}_2\text{OH}$  on Co catalysts.<sup>51</sup> For the comparison between hcp-Co and fcc-Co, hcp-Co was found to be superior for  $\text{NH}_3$  production, attributing to it showing facile proton and electron transfer during the key steps in  $\text{NH}_3$  formation (Fig. 4(l)). The energetic barriers for key steps such as the hydrogenation of  $^*\text{NO}$  was lower on hcp-Co compared to fcc-Co. Additionally, hcp-Co exhibited a charge-transfer coefficient larger than that of fcc-Co, and NO accepted more electrons upon adsorption from hcp-Co. The lateral suppression effect from  $^*\text{NO}$  was also stronger on hcp-Co. The calculated selectivity of  $\text{NH}_3$  production on hcp-Co was consistent with experimental results. Co-SA was highly selective for  $\text{NH}_2\text{OH}$

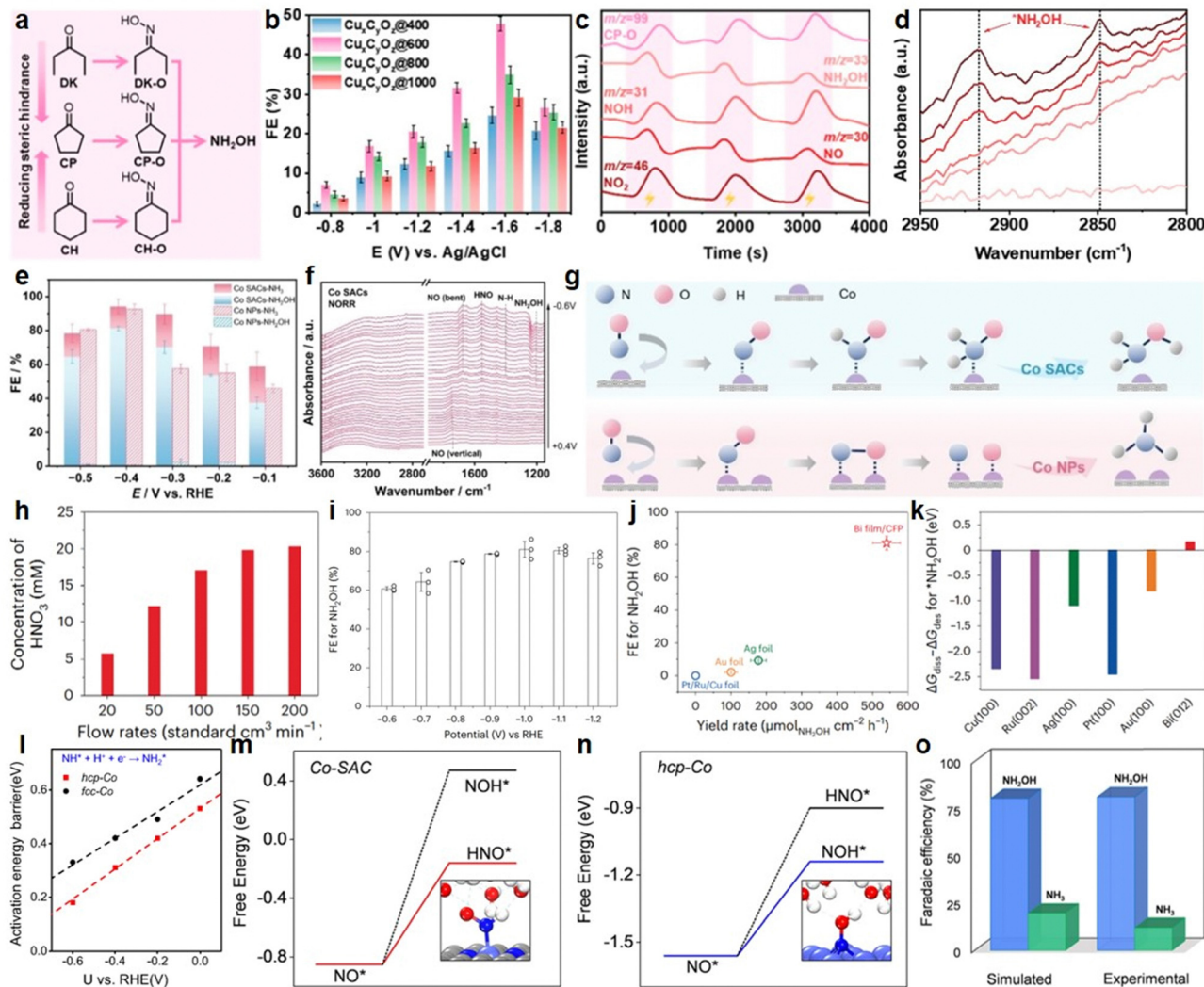


Fig. 4 (a) Illustration of  $\text{NH}_2\text{OH}$  synthesis mediated by ketone. (b) Oxime FE of  $\text{Cu}_x\text{C}_y\text{O}_z$  catalysts. (c) Online DEMS and (d) *in situ* ATR-FTIR of  $\text{NO}_3^-$  reduction with a ketone mediator. Reproduced with permission from ref. 48. (e) FE of  $\text{NH}_2\text{OH}$  and  $\text{NH}_3$  on Co SACs and Co NPs catalysts. (f) *In situ* ATR-FTIR and (g) reaction pathways of  $\text{NH}_2\text{OH}$  generation on Co SACs. Reproduced with permission from ref. 49. (h)  $\text{NO}_3^-$  concentration under different flow rates of air. (i)  $\text{NH}_2\text{OH}$  FE of (i) Bi film/CFP and (j) other metal electrodes. (k) Energy diagram of  $\text{NH}_2\text{OH}$  absorption on different metal. Reproduced with permission from ref. 50. (l) Energy barriers of  $^*\text{NO}$  hydrogenation to  $^*\text{NOH}$  over hcp-Co and fcc-Co. Free energy diagram for  $^*\text{NO}$  hydrogenation to  $^*\text{HNO}$  or  $^*\text{NOH}$  on (m) Co-SAC and (n) hcp-Co. (o) Simulated and experimental  $\text{NH}_2\text{OH}$  FE on SAC-Co. Reproduced with permission from ref. 51.

production *via*  $^*\text{HNO}$ . The electronic structure of Co-SAC was more localized, resulting in a positively charged catalytic active site. This led to weaker adsorption of intermediates compared to hcp-Co. The reaction mechanism on Co-SAC for  $\text{NH}_2\text{OH}$  production was different from that on hcp-Co and fcc-Co. The  $^*\text{NO}$  protonation to  $^*\text{HNO}$  on Co-SAC was a combination of partial electron transfer and proton transfer process (Fig. 4(m)), while on hcp-Co, the adsorption of  $^*\text{NO}$  and  $^*\text{NOH}$  production was a sequential electron and proton transfer process (Fig. 4(n)). As a result, Co-SAC and bulk Co led to the formation of  $\text{NH}_2\text{OH}$  and  $\text{NH}_3$ , respectively, as is shown in Fig. 4(o).

Recently, we proposed an electrocatalytic system for upgrading  $\text{NO}_3^-$  to  $\text{N}_2\text{H}_4$ , involving electrochemical  $\text{NO}_3^-$  upgrading to  $\text{NH}_3$ , followed by ketone-mediated  $\text{NH}_3$  to  $\text{N}_2\text{H}_4$ , achieving an overall selectivity of 88.7% for the conversion of  $\text{NO}_3^-$  to

$\text{N}_2\text{H}_4$ .<sup>52</sup> Diphenyl ketone (DPK) emerged as an optimal mediator, facilitating controlled N-N coupling due to its steric and conjugation effects. The acetonitrile solvent stabilized and activated key imine intermediates through hydrogen bonding. The imine intermediates formed on  $\text{WO}_3$  catalyst acted as pivotal monomers to drive controlled N-N coupling with high selectivity, which was facilitated by lattice oxygen-mediated dehydrogenation on  $\text{WO}_3$  catalyst.

### 3.4 Organonitrogen chemicals

While ammonia has long been the primary nitrogen source for the production of organonitrogen compounds, such as amino acids, amides, and amines, the electrocatalytic upgrading of  $\text{NO}_x$  offers distinct advantages by utilizing nitrogenous pollutants as feedstocks. This approach not only mitigates

## Highlight

environmental pollution but also converts  $\text{NO}_x$  wastes into high-value chemicals that are crucial for various industries, including pharmaceuticals, agriculture, and polymers. In contrast to conventional processes, which often require harsh reagents and high-temperature conditions,  $\text{NO}_x$  upgrading *via* electrocatalysis can provide a more energy-efficient and environmentally friendly alternative.

**Oxime.** Our group reported the synthesis of cyclohexanone oxime using air-derived  $\text{NO}_x$  as the nitrogen source (Fig. 5(a)), in which the electrocatalytic reactions were conducted on  $\text{Cu}/\text{TiO}_2$  catalyst and achieved a high performance with a cyclohexanone oxime formation rate of  $20.1 \text{ mg h}^{-1} \text{ cm}^{-2}$  and a FE of 51.4%.<sup>53</sup> The selectivity of cyclohexanone oxime was  $>99.9\%$  based on cyclohexanone. The reaction involved plasma-assisted air-to- $\text{NO}_x$  (Fig. 5(b)) and co-electrolysis of  $\text{NO}_x$  and cyclohexanone (Fig. 5(c)). Cyclohexanone oxime formed through the reaction

between an  $\text{NH}_2\text{OH}$  intermediate generated from  $\text{NO}_x$  reduction and cyclohexanone. The Li group presented the conversion of  $\text{NO}_x$  into oxime ethers using  $\text{MgO}$  nanoparticles anchored in self-standing carbon-nanofibers membrane ( $\text{MgO-SCM}$ ) derived from  $\text{Mg-MOF/polymer}$ , which showed excellent performance with a selectivity of 93% and FE up to 65.1% for 4-cyanobenzaldoxime production.<sup>35</sup> The tandem electrocatalytic reduction reaction is a three-step process. First,  $\text{NO}$  was converted into  $\text{NH}_2\text{OH}$ , which then spontaneously attacked aldehydes to form oximes. The  $\text{MgO-SCM}$  played a critical role in the kinetic control of the electrocatalytic process. Due to the preferential adsorption of  $\text{NO}$  over  $\text{OH}$  ions by  $\text{MgO}$  nanoparticles, the catalyst favoured the production of  $\text{NH}_2\text{OH}$ , especially in the presence of aldehydes. Its weak hydrogenation capacity reduced the formation of alcohol and amine from aldehydes and oximes, respectively, leading to high productivity and energy efficiency.

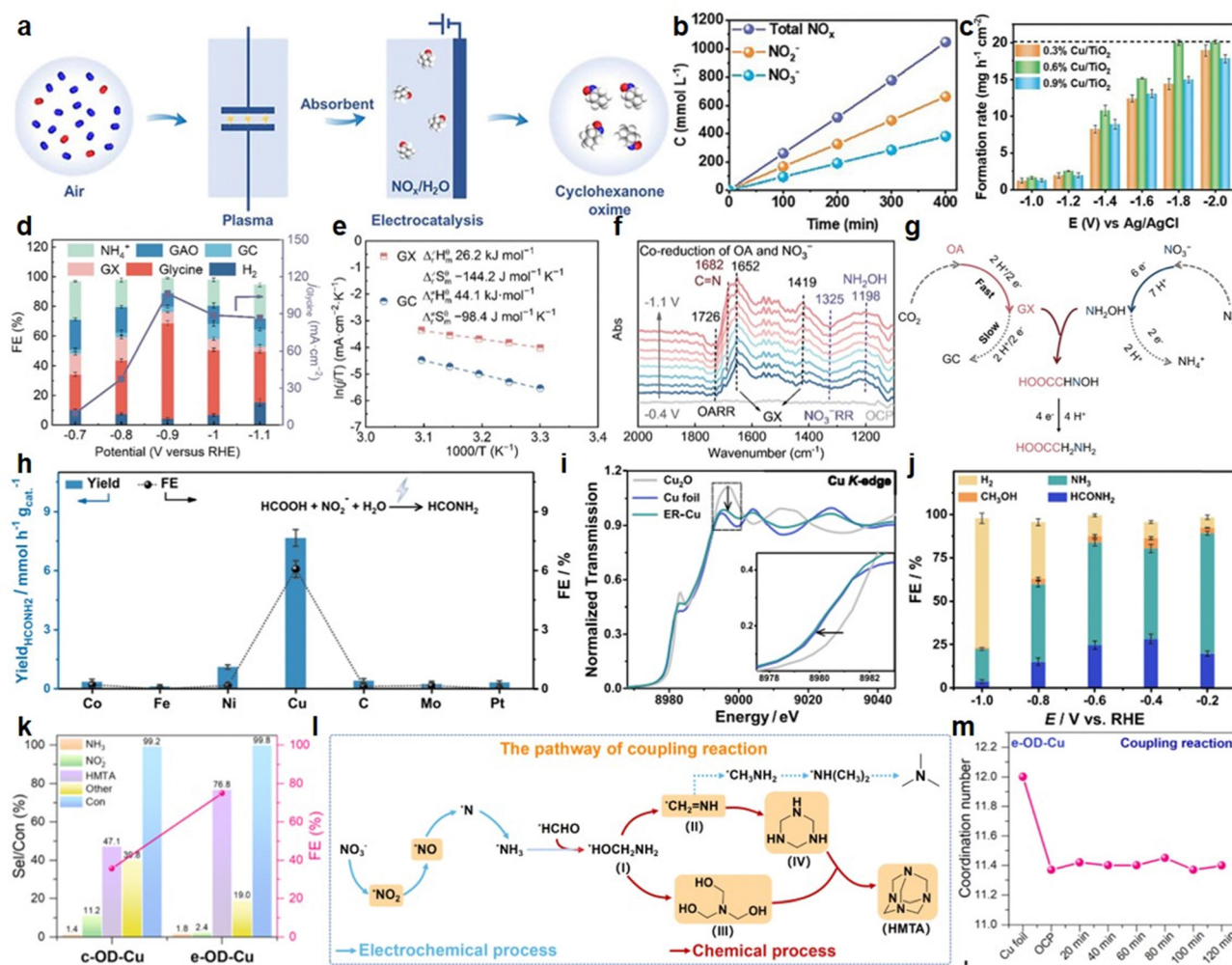


Fig. 5 (a) Illustration of the cyclohexanone oxime synthesis of with air. (b) Concentration of  $\text{NO}_3^-$  and  $\text{NO}_2^-$  generated from air oxidation for different time. (c) FE of cyclohexanone on  $\text{Cu}/\text{TiO}_2$  catalysts. Reproduced with permission from ref. 53. (d) Performance of Fe-N-C-700 for electrosynthesis of glycine and the corresponding (e) Eyring plots. (f) *In situ* ATR-FTIR during the generation of glycine. (g) Reaction pathways of glycine formation. Reproduced with permission from ref. 54. (h) FE of formamide on different metal foil electrode. (i) Extended XANES spectra of Cu K-edge of ER-Cu catalyst. (j) Electrochemical performance of formamide generation on ER-Cu. Reproduced with permission from ref. 55. (k) Electrochemical performance of HMTA HMTA on c-OD-Cu and e-OD-Cu and (l) the corresponding reaction pathway. (m) The coordination number of Cu in e-OD-Cu during electroreduction. Reproduced with permission from ref. 56.

**Amino acid.** Our group demonstrated the electrosynthesis of glycine using atomically dispersed Fe–N–C catalyst, which shows excellent performance and a glycine selectivity of 70.7% was achieved (Fig. 5(d)).<sup>54</sup> The reaction was enabled by the reductive coupling of oxalic acid and  $\text{NO}_x$ . The  $\text{FeN}_3\text{C}$  structure and pyrrolic nitrogen in Fe–N–C-700 played crucial roles through facilitating the reduction of oxalic acid to glyoxylic acid (Fig. 5(e)), which was important for producing glyoxylic acid oxime and glycine (Fig. 5(f)). The synergy between the  $\text{FeN}_3\text{C}$  structure and pyrrolic nitrogen creates a local reactant-rich environment, favouring further coupling reactions (Fig. 5(g)).  $\text{FeN}_3\text{C}$  also reduced the energy barrier of  $^*\text{HOOCHNH}_2$  intermediate formation, accelerating the conversion of glyoxylic acid oxime to glycine. The Zhang group recently proposed the electrocatalytic synthesis of amino acids from NO and  $\alpha$ -keto acids on oxide-derived Ag (OD-Ag) with low-coordination sites.<sup>57</sup> In one-pot reaction, it achieved a FE of 17.0% and a yield rate of  $11.45 \text{ mmol h}^{-1} \text{ g}^{-1}$  for alanine synthesis. However, the one-pot system had limitations due to the mismatch of pyruvate oxime formation and reduction steps. Mechanistic studies revealed a cascade  $\text{NO} \rightarrow \text{NH}_2\text{OH} \rightarrow$  pyruvate oxime  $\rightarrow$  alanine pathway. To overcome these issues, a spatially decoupled two-pot electrosynthesis system using flow reactors loaded with OD-Ag was designed. This decoupled system delivered  $3.85 \text{ g}$  of easily purified alanine with a total FE of 70% and a purity of  $>98\%$  at  $100 \text{ mA cm}^{-2}$ . The techno-economic analysis and solar-energy-powered electrosynthesis system demonstrated the potential of this strategy, which was also suitable for synthesizing other amino acids.

**Amides.** Zhang and co-workers reported the upgrading of formic acid to formamide *via* coupling  $\text{NO}_2^-$  co-reduction.<sup>55</sup> Among the screened electrocatalysts, Cu showed the highest performance (Fig. 5(h)). By preparing low-coordinated Cu nanocubes (ER-Cu) (Fig. 5(i)) through electrochemical reduction of  $\text{Cu}_2\text{O}$  nanocubes, an optimal formamide FE of 29.7% was achieved, with a selectivity from formic acid to formamide up to 90.0% (Fig. 5(j)). C–N bond formation occurred through coupling  $^*\text{CHO}$  and  $^*\text{NH}$  intermediates. Ma *et al.* achieved the electrochemical conversion of  $\text{CO}_2$  and  $\text{NO}_2^-$  to acetamide using copper nanoparticles.<sup>58</sup> The electrochemical performance showed that acetamide formation on Cu nanoparticles reached to  $20 \text{ mA cm}^{-2}$  and  $80 \text{ mA cm}^{-2}$  at  $0.5 \text{ mol L}^{-1} \text{ KOH}$  and  $1.0 \text{ mol L}^{-1} \text{ KOH}$ , respectively. Reduction of  $\text{CO}_2$  and  $\text{NO}_2^-$  first proceeded separately to generate acetaldehyde and  $\text{NH}_2\text{OH}$ . They then underwent a nucleophilic addition reaction to form acetaldoxime, which was further dehydrogenated and dehydroxylated to form acetonitrile. Finally, acetonitrile was hydrolysed in the alkaline bulk electrolyte to form the final product acetamide.

**Amine.** Recently, the Wang group conducted the electrocatalytic coupling of  $\text{NO}_3^-$  and formaldehyde for the synthesis of hexamethylenetetramine (HMTA) on electrochemical oxidation-derived copper (e-OD-Cu) with Cu vacancies.<sup>58</sup> e-OD-Cu achieved an HMTA yield of 76.8% and a FE of 74.9% (Fig. 5(k)). The reaction pathway of HMTA synthesis on e-OD-Cu involved a tandem electrochemical-chemical process (Fig. 5(l)). Cu vacancies, which

was stable on the surface of e-OD-Cu during electroreduction (Fig. 5(m)), enhanced substrate adsorption and inhibit the further hydrogenation of  $\text{C}=\text{N}$  species. Wang *et al.* demonstrated the electrochemical conversion of carbon dioxide and  $\text{NO}_3^-$  to methylamine using a cobalt  $\beta$ -tetraaminophthalocyanine molecular catalyst supported on carbon nanotubes.<sup>59</sup> Under ambient conditions, methylamine was generated in a highly cooperative one-pot process with an overall FE of 13% and showed no performance decay for at least 16 h of continuous operation. Electrochemical  $\text{CO}_2$  reduction and  $\text{NO}_2^-$  reduction first proceed independently until  $\text{HCHO}$  and  $\text{NH}_2\text{OH}$  were formed. C–N bond-forming step was enabled by the spillover of  $\text{NH}_2\text{OH}$  from  $\text{NO}_3^-$  reduction and its subsequent condensation with formaldehyde from  $\text{CO}_2$  reduction, yielding formaldoxime, which was further electrochemically reduced to target methylamine product.

**Urea.** Yu and co-workers reported indium hydroxide ( $\text{In(OH)}_3$ ) with well-defined  $\{100\}$  facets as the catalyst for the electrocatalytic synthesis of urea from  $\text{NO}_3^-$  and  $\text{CO}_2$ , which achieved an average urea yield of  $533.1 \mu\text{g h}^{-1} \text{ mg}_{\text{cat}}^{-1}$ , with a FE of 53.4%, nitrogen selectivity of 82.9% and carbon selectivity of approximately 100%.<sup>60</sup> The direct C–N coupling of  $^*\text{NO}$  and  $^*\text{CO}_2$  intermediates occurred on the  $\{100\}$  facets of  $\text{In(OH)}_3$ . The  $^*\text{NO}$  intermediate was formed through the thermodynamically spontaneous reduction of  $\text{NO}_3^-$ . The lower energy barrier for the direct coupling of  $^*\text{NO}$  and  $^*\text{CO}_2$  compared to the protonation of  $^*\text{NO}$  or  $^*\text{CO}_2$  separately led to high selectivity. Additionally,  $^*\text{CO}_2$  can suppress the HER by inducing an n–p transformation in the surface semiconducting behaviour of  $\text{In(OH)}_3$ . The Sargent group utilized Zn/Cu hybrid catalyst for co-electrolysis of  $\text{NO}_3^-$  and  $\text{CO}_2$  to synthesize urea.<sup>61</sup> At wastewater-level nitrate concentrations, a FE of 75% was achieved, with a urea production rate of  $16 \mu\text{mol h}^{-1} \text{ cm}^{-2}$ .  $^*\text{CO}_2\text{NO}_2$  preferentially forms on Zn sites, and the ensuing protonation step to form  $^*\text{COOHNH}_2$  benefited from a lowered reaction energy on nearby Cu sites. He *et al.* provided insights into the co-reduction of  $\text{CO}_2$  and  $\text{NO}_3^-$  for sustainable urea synthesis under pulsed electrolysis.<sup>62</sup> An iron tetraphenylporphyrin molecular electrocatalyst (Fe-TPP/CNTs) achieved a maximum FE of 27.70% for urea under pulsed electrolysis, which increased the local concentration of  $\text{CO}_2$  and  $\text{NO}_3^-$  but reduced the local pH to enrich  $^*\text{CO}$  and  $^*\text{NH}_2$  intermediates favoured by C–N coupling, creating a favourable local environment for urea generation while suppressing competing reactions. Liao *et al.* designed  $\gamma\text{-Fe}_2\text{O}_3@\text{Ni-HITP}$ , consisting of ultrasmall  $\gamma\text{-Fe}_2\text{O}_3$  nanoparticles ( $<2 \text{ nm}$ ) encapsulated in the pores of a conductive Ni-HITP metal–organic framework, which exhibited excellent electrocatalytic performance for urea synthesis, achieving a FE of 67.2%, a current density of  $-90 \text{ mA cm}^{-2}$ , and a high yield rate of  $20.4 \text{ g h}^{-1} \text{ g}_{\text{cat}}^{-1}$ .<sup>63</sup>  $\text{Fe}^{\text{III}}$  species in the  $\gamma\text{-Fe}_2\text{O}_3$  nanoparticles showed high activity, generating key intermediates  $^*\text{NH}_2$  and  $^*\text{COOH}$ . Pairs of adjacent  $\text{Fe}^{\text{III}}$  in the  $\gamma\text{-Fe}_2\text{O}_3$  nanoparticles acted as highly active catalytic sites for catalysing the C–N coupling between  $^*\text{NH}_2$  and  $^*\text{COOH}$ , forming the subsequent key intermediate  $^*\text{CONH}$ , contributing to the high performance for urea production.

The progress outlined above demonstrates that  $\text{NH}_2\text{OH}$  is widely available direct nitrogen source, generated from  $\text{NO}_x$ ,

## Highlight

and capable of undergoing carbon–nitrogen condensation with ketones and aldehydes. We propose that NH<sub>2</sub>OH can serve as a useful intermediate in carbon–nitrogen condensation reactions for two key reasons. First, NH<sub>2</sub>OH exhibits higher nucleophilicity than other nitrogen-containing species generated from NO<sub>x</sub> such as NH<sub>3</sub>. Second, NH<sub>2</sub>OH possesses an eight-electron stable structure, which confers greater stability and longer lifetime compared to other intermediates, such as \*NH<sub>2</sub>, \*NH, and \*N, allowing NH<sub>2</sub>OH to facilitate subsequent reactions.

In addition, product separation and purification of organic products are critical for advancing the practical applications of electrocatalytic NO<sub>x</sub> upgrading technology in large-scale systems. For example, Li *et al.* demonstrated the successful purification of amino acids with 93% purity using a simple freeze-drying technique,<sup>64</sup> while cyclohexanone oxime was obtained with a 95% yield following straightforward separation and steam drying.<sup>65</sup> These advances highlight the potential for scalable, cost-effective separation methods that can support the industrial application of NO<sub>x</sub> upgrading technologies.

## 4. Summary and outlook

### 4.1 Electrocatalytic systems coupled with physical fields

The future of electrocatalytic NO<sub>x</sub> upgrading lies in the integration of multiple physical fields, including light, heat, and magnetism, to enhance the performance and efficiency of catalytic systems. By harnessing these physical fields, we can design novel electrocatalytic systems that provide more efficient activation and conversion of nitrogenous intermediates. In-depth exploration of the mechanisms by which these physical fields interact with nitrogenous intermediates is essential for optimizing catalytic processes and boosting NO<sub>x</sub> upgrading.

### 4.2 *In situ* characterization techniques

A comprehensive understanding of the reaction pathways of electrocatalytic NO<sub>x</sub> upgrading systems is vital to achieving greater efficiency. To this end, developing advanced *in situ* characterization techniques is of great importance. These techniques will allow researchers to observe the behaviour of catalysts and intermediates under in real time, revealing critical insights into their interaction mechanisms. Harnessing these insights, we can fine-tune electrocatalytic processes to achieve enhanced performance and novel product outcomes.

### 4.3 Sustainable pathways for renewable resource utilization

Another essential direction for NO<sub>x</sub> upgrading is the development of novel catalytic pathways. We can pioneer complex catalytic systems capable of converting raw materials into high-value products with greater efficiency and sustainability. This concept can be further elaborated by designing a series of integrated systems that combine established thermal catalysis or biodegradation technologies with electrocatalytic conversion processes. Additionally, the creation of new catalyst-solvent-device systems is crucial for enabling these efficient conversions, further bridging the gap between upstream raw material supply and downstream product synthesis.

By pushing forward in these directions, we can unlock new potentials in electrocatalytic NO<sub>x</sub> upgrading and we believe that electrocatalytic NO<sub>x</sub> upgrading systems can pave the way for the application of clean energy and renewable nitrogen resources.

## Author contributions

S. J., X. S., and B. H. wrote the manuscript. X. S. and B.H. supervised the project.

## Data availability

No primary research results, software or code have been included and no new data were generated or analysed as part of this review.

## Conflicts of interest

There are no conflicts to declare.

## Acknowledgements

The work was supported by the National Natural Science Foundation of China (22293015 and 22121002) and Photon Science Center for Carbon Neutrality.

## Notes and references

- 1 P. Gao, L. Zhong, B. Han, M. He and Y. Sun, *Angew. Chem., Int. Ed.*, 2022, **61**, e202210095.
- 2 M. He, Y. Sun and B. Han, *Angew. Chem., Int. Ed.*, 2013, **52**, 9620–9633.
- 3 M. He, Y. Sun and B. Han, *Angew. Chem., Int. Ed.*, 2022, **61**, e202112835.
- 4 Z. Cen, X. Han, L. Lin, S. Yang, W. Han, W. Wen, W. Yuan, M. Dong, Z. Ma, F. Li, Y. Ke, J. Dong, J. Zhang, S. Liu, J. Li, Q. Li, N. Wu, J. Xiang, H. Wu, L. Cai, Y. Hou, Y. Cheng, L. L. Daemen, A. J. Ramirez-Cuesta, P. Ferrer, D. C. Grinter, G. Held, Y. Liu and B. Han, *Nat. Chem.*, 2024, **16**, 871–880.
- 5 R. Wu, Q. Meng, J. Yan, Z. Zhang, B. Chen, H. Liu, J. Tai, G. Zhang, L. Zheng, J. Zhang and B. Han, *Nat. Catal.*, 2024, **7**, 702–718.
- 6 X. Wu, J. Du, Y. Gao, H. Wang, C. Zhang, R. Zhang, H. He, G. Lu and Z. Wu, *Chem. Soc. Rev.*, 2024, **53**, 8379–8423.
- 7 F. Wang, J. D. Harindintwalli, Z. Yuan, M. Wang, F. Wang, S. Li, Z. Yin, L. Huang, Y. Fu, L. Li, S. X. Chang, L. Zhang, J. Rinklebe, Z. Yuan, Q. Zhu, L. Xiang, D. C. W. Tsang, L. Xu, X. Jiang, J. Liu, N. Wei, M. Kästner, Y. Zou, Y. S. Ok, J. Shen, D. Peng, W. Zhang, D. Barceló, Y. Zhou, Z. Bai, B. Li, B. Zhang, K. Wei, H. Cao, Z. Tan, L.-B. Zhao, X. He, J. Zheng, N. Bolan, X. Liu, C. Huang, S. Dietmann, M. Luo, N. Sun, J. Gong, Y. Gong, F. Brahusi, T. Zhang, C. Xiao, X. Li, W. Chen, N. Jiao, J. Lehmann, Y.-G. Zhu, H. Jin, A. Schäffer, J. M. Tiedje and J. M. Chen, *Innovation*, 2021, **2**, 100180.
- 8 Y. Wang, Y. Qin, W. Li, Y. Wang, L. Zhu, M. Zhao and Y. Yu, *Trans. Tianjin Univ.*, 2023, **29**, 275–283.
- 9 S. Jia, L. Wu, H. Liu, R. Wang, X. Sun and B. Han, *Angew. Chem., Int. Ed.*, 2024, **63**, e202400033.
- 10 D. Wang, X. F. Lu, D. Luan and X. W. Lou, *Adv. Mater.*, 2024, **36**, 2312645.
- 11 P. Liao, J. Kang, R. Xiang, S. Wang and G. Li, *Angew. Chem., Int. Ed.*, 2024, **63**, e202311752.
- 12 Y. Wang, C. Wang, M. Li, Y. Yu and B. Zhang, *Chem. Soc. Rev.*, 2021, **50**, 6720–6733.
- 13 H. Liu, S. Jia, L. Wu, L. He, X. Sun and B. Han, *Innov. Mater.*, 2024, **2**, 100058.

14 Y. Zhong, H. Xiong, J. Low, R. Long and Y. Xiong, *eScience*, 2023, **3**, 100086.

15 H. Yao, M.-Y. Wang, C. Yue, B. Feng, W. Ji, C. Qian, S. Wang, S. Zhang and X. Ma, *Trans. Tianjin Univ.*, 2023, **29**, 254–274.

16 L. Zhang, X. Sun and B. Han, *Sci. Bull.*, 2024, **69**, 563–565.

17 D. Wang, J. Mao, C. Zhang, J. Zhang, J. Li, Y. Zhang and Y. Zhu, *eScience*, 2023, **3**, 100119.

18 H. H. Wong, M. Sun, T. Wu, C. H. Chan, L. Lu, Q. Lu, B. Chen and B. Huang, *eScience*, 2024, **4**, 100140.

19 L. Xu, R. Iqbal, Y. Wang, S. Taimoor, L. Hao, R. Dong, K. Liu, J. Texter and Z. Sun, *Innov. Mater.*, 2024, **2**, 100060.

20 W. Li, H. Jiang, X. Zhang, B. Lei, L. Li, H. Zhou and M. Zhong, *J. Am. Chem. Soc.*, 2024, **146**, 21968–21976.

21 Y. Yin, Y. Peng, M. Zhou, P. Zhang, Y. Cheng, P. Chen, X. Xing, X. Ma, Q. Zhu, X. Sun, Q. Qian, X. Kang and B. Han, *Sci. Bull.*, 2023, **68**, 2362–2369.

22 J. Feng, L. Wu, X. Song, L. Zhang, S. Jia, X. Ma, X. Tan, X. Kang, Q. Zhu, X. Sun and B. Han, *Nat. Commun.*, 2024, **15**, 4821.

23 A. Li, P. Zhang, E. Kan and J. Gong, *eScience*, 2024, **4**, 100157.

24 G. Xie, W. Guo, Z. Fang, Z. Duan, X. Lang, D. Liu, G. Mei, Y. Zhai, X. Sun and X. Lu, *Angew. Chem., Int. Ed.*, 2024, e202412568.

25 L. Zhou and R. Lv, *J. Energy Chem.*, 2022, **70**, 310–331.

26 S. Jia, L. Wu, L. Xu, X. Sun and B. Han, *Ind. Chem. Mater.*, 2023, **1**, 93–105.

27 K. Wang, R. Mao, R. Liu, J. Zhang, H. Zhao, W. Ran and X. Zhao, *Nat. Water*, 2023, **1**, 1068–1078.

28 F.-Y. Chen, A. Elgazzar, S. Pecaut, C. Qiu, Y. Feng, S. Ashokkumar, Z. Yu, C. Sellers, S. Hao, P. Zhu and H. Wang, *Nat. Catal.*, 2024, **7**, 1032–1043.

29 Z. Wu, X. Kang, S. Wang, Y. Song, F. Xie, X. Duan and J. Yang, *Adv. Funct. Mater.*, 2024, 2406917.

30 Y. Fang, M. Li, Y. Gao, Y. Wen and B. Shan, *Angew. Chem., Int. Ed.*, 2024, e202415729.

31 M. Wang, S. Li, Y. Gu, W. Xu, H. Wang, J. Sun, S. Chen, Z. Tie, J.-L. Zuo, J. Ma, J. Su and Z. Jin, *J. Am. Chem. Soc.*, 2024, **146**, 20439–20448.

32 J. Shao, H. Jing, P. Wei, X. Fu, L. Pang, Y. Song, K. Ye, M. Li, L. Jiang, J. Ma, R. Li, R. Si, Z. Peng, G. Wang and J. Xiao, *Nat. Energy*, 2023, **8**, 1273–1283.

33 J. Zhou, Y. Zhu, K. Wen, F. Pan, H. Ma, J. Niu, C. Wang and J. Zhao, *Environ. Sci. Technol.*, 2024, **58**, 4824–4836.

34 Y. Fan, X. Wang, C. Butler, A. Kankam, A. Belgada, J. Simon, Y. Gao, E. Chen and L. R. Winter, *Nat. Water*, 2024, **2**, 684–696.

35 S. Wang, R. Xiang, P. Liao, J. Kang, S. Li, M. Mao, L. Liu and G. Li, *Angew. Chem., Int. Ed.*, 2024, **63**, e202405553.

36 Y. Zhou, L. Zhang, Z. Zhu, M. Wang, N. Li, T. Qian, C. Yan and J. Lu, *Angew. Chem., Int. Ed.*, 2024, **63**, e202319029.

37 L. Wu, S. Jia, L. Zhang, R. Wang, J. Feng, X. Sun and B. Han, *Sci. China: Chem.*, 2024, **67**, 1969–1975.

38 L. Wu, J. Feng, L. Zhang, S. Jia, X. Song, Q. Zhu, X. Kang, X. Xing, X. Sun and B. Han, *Angew. Chem., Int. Ed.*, 2023, **62**, e202307952.

39 Y. Huang, C. He, C. Cheng, S. Han, M. He, Y. Wang, N. Meng, B. Zhang, Q. Lu and Y. Yu, *Nat. Commun.*, 2023, **14**, 7368.

40 Y. Xu, C. Cheng, J. Zhu, B. Zhang, Y. Wang and Y. Yu, *Angew. Chem., Int. Ed.*, 2024, **63**, e202400289.

41 W. Wen, S. Fang, Y. Zhou, Y. Zhao, P. Li and X.-Y. Yu, *Angew. Chem., Int. Ed.*, 2024, **63**, e202408382.

42 L. Zhou, X. Chen, S. Zhu, K. You, Z.-J. Wang, R. Fan, J. Li, Y. Yuan, X. Wang, J. Wang, Y. Chen, H. Jin, S. Wang and J.-J. Lv, *Angew. Chem., Int. Ed.*, 2024, **63**, e202401924.

43 F. Hong, X. Su, Y. Fang, X. He and B. Shan, *J. Am. Chem. Soc.*, 2024, **146**, 25200–25210.

44 Y. Wang, H. He, H. Lv, F. Jia and B. Liu, *Nat. Commun.*, 2024, **15**, 6761.

45 Y. Bu, W. Yu, Q. Yang, W. Zhang, Q. Sun, W. Wu, P. Cui, C. Wang and G. Gao, *Environ. Sci. Technol.*, 2024, **58**, 12708–12718.

46 H. Xu, Y. Ma, J. Chen, W.-X. Zhang and J. Yang, *Chem. Soc. Rev.*, 2022, **51**, 2710–2758.

47 Y. Li, J. Ma, T. D. Waite, M. R. Hoffmann and Z. Wang, *Environ. Sci. Technol.*, 2021, **55**, 10695–10703.

48 S. Jia, L. Wu, X. Tan, J. Feng, X. Ma, L. Zhang, X. Song, L. Xu, Q. Zhu, X. Kang, X. Sun and B. Han, *J. Am. Chem. Soc.*, 2024, **146**, 10934–10942.

49 J. Zhou, S. Han, R. Yang, T. Li, W. Li, Y. Wang, Y. Yu and B. Zhang, *Angew. Chem., Int. Ed.*, 2023, **62**, e202305184.

50 X. Kong, J. Ni, Z. Song, Z. Yang, J. Zheng, Z. Xu, L. Qin, H. Li, Z. Geng and J. Zeng, *Nat. Sustain.*, 2024, **7**, 652–660.

51 P. Guo, D. Luan, H. Li, L. Li, S. Yang and J. Xiao, *J. Am. Chem. Soc.*, 2024, **146**, 13974–13982.

52 S. Jia, L. Zhang, H. Liu, R. Wang, X. Jin, L. Wu, X. Song, X. Tan, X. Ma, J. Feng, Q. Zhu, X. Kang, Q. Qian, X. Sun and B. Han, *Nat. Commun.*, 2024, **15**, 8567.

53 S. Jia, X. Tan, L. Wu, X. Ma, L. Zhang, J. Feng, L. Xu, X. Song, Q. Zhu, X. Kang, X. Sun and B. Han, *Chem. Sci.*, 2023, **14**, 13198–13204.

54 Y. Cheng, S. Liu, J. Jiao, M. Zhou, Y. Wang, X. Xing, Z. Chen, X. Sun, Q. Zhu, Q. Qian, C. Wang, H. Liu, Z. Liu, X. Kang and B. Han, *J. Am. Chem. Soc.*, 2024, **146**, 10084–10092.

55 M. Li, Y. Wu, B.-H. Zhao, C. Cheng, J. Zhao, C. Liu and B. Zhang, *Nat. Catal.*, 2023, **6**, 906–915.

56 Y. Pan, Y. Zou, C. Ma, T. T. Nga, Q. An, R. Miao, Z. Xia, Y. Fan, C.-L. Dong, Q. Liu and S. Wang, *J. Am. Chem. Soc.*, 2024, **146**, 19572–19579.

57 M. Li, Y. Wu, B.-H. Zhao, C. Cheng, J. Zhao, C. Liu and B. Zhang, *Nat. Catal.*, 2023, **6**, 906–915.

58 S. Kuang, T. Xiao, H. Chi, J. Liu, C. Mu, H. Liu, S. Wang, Y. Yu, T. J. Meyer, S. Zhang and X. Ma, *Angew. Chem., Int. Ed.*, 2024, **63**, e202316772.

59 Y. Wu, Z. Jiang, Z. Lin, Y. Liang and H. Wang, *Nat. Sustain.*, 2021, **4**, 725–730.

60 C. Lv, L. Zhong, H. Liu, Z. Fang, C. Yan, M. Chen, Y. Kong, C. Lee, D. Liu, S. Li, J. Liu, L. Song, G. Chen, Q. Yan and G. Yu, *Nat. Sustain.*, 2021, **4**, 868–876.

61 Y. Luo, K. Xie, P. Ou, C. Lavallais, T. Peng, Z. Chen, Z. Zhang, N. Wang, X.-Y. Li, I. Grigioni, B. Liu, D. Sinton, J. B. Dunn and E. H. Sargent, *Nat. Catal.*, 2023, **6**, 939–948.

62 Q. Hu, W. Zhou, S. Qi, Q. Huo, X. Li, M. Lv, X. Chen, C. Feng, J. Yu, X. Chai, H. Yang and C. He, *Nat. Sustain.*, 2024, **7**, 442–451.

63 D.-S. Huang, X.-F. Qiu, J.-R. Huang, M. Mao, L. Liu, Y. Han, Z.-H. Zhao, P.-Q. Liao and X.-M. Chen, *Nat. Synth.*, 2024, **3**, 1404–1413.

64 J. Xian, S. Li, H. Su, P. Liao, S. Wang, R. Xiang, Y. Zhang, Q. Liu and G. Li, *Angew. Chem., Int. Ed.*, 2023, **62**, e202306726.

65 Y. Wu, W. Chen, Y. Jiang, Y. Xu, B. Zhou, L. Xu, C. Xie, M. Yang, M. Qiu, D. Wang, Q. Liu, Q. Liu, S. Wang and Y. Zou, *Angew. Chem., Int. Ed.*, 2023, **62**, e202305491.